Origins of bad-metal conductivity and the insulator–metal transition in the rare-earth nickelates

R. Jaramillo[1]*[†], Sieu D. Ha[1], D. M. Silevitch[2] and Shriram Ramanathan[1]

For most metals, increasing temperature (T) or disorder hastens electron scattering. The electronic conductivity (σ) decreases as T rises because electrons are more rapidly scattered by lattice vibrations. The value of σ decreases as disorder increases because electrons are more rapidly scattered by imperfections in the material. This is the scattering rate hypothesis, which has guided our understanding of metal conductivity for over a century. However, for so-called bad metals with very low σ this hypothesis predicts scattering rates so high as to conflict with Heisenberg's uncertainty principle[1,2]. Bad-metal conductivity has remained a puzzle since its initial discovery in the 1980s in high-temperature superconductors. Here we introduce the rare-earth nickelates (RNiO$_3$, R = rare-earth) as a class of bad metals. We study SmNiO$_3$ thin films using infrared spectroscopy while varying T and disorder. We show that the interaction between lattice distortions and Ni–O covalence explains bad-metal conductivity and the insulator–metal transition. This interaction shifts spectral weight over the large energy scale established by the Ni–O orbital interaction, thus enabling very low σ without violating the uncertainty principle.

The Drude model describes the dependence of σ on the lifetime (τ) between scattering events, the free carrier concentration (n), the carrier effective mass (m^*), and the elementary charge (q): $\sigma = nq^2\tau/m^*$. For metals the electron–phonon scattering rate increases with T, producing a linear dependence $\sigma^{-1} \propto \tau^{-1} \propto T$ at sufficiently high T. Elementary quantum theory dictates that this relationship cannot continue indefinitely. According to Heisenberg's uncertainty principle the uncertainty ΔE of a particle's energy is inversely proportional to its lifetime: $\Delta E = h/\tau$. Therefore there exists a minimum τ below which the concept of a well-defined quasiparticle energy becomes unphysical. This lower bound on τ implies a minimum metallic conductivity (σ_{MIR}), which is called the Mott–Ioffe–Regel (MIR) limit[1,2]. Most metals reach their melting temperature well before the MIR limit. There are some so-called 'saturating' metals for which $\sigma(T)$ approaches σ_{MIR} and saturates, thus validating the MIR limit. However, in bad metals the relationship $\sigma^{-1} \propto T$ continues unabated through the MIR limit. According to the Drude model these metals have lifetimes so short that the quasiparticles should be unstable (that is, decohere), producing an insulating state, and yet the transport properties remain metallic. Bad-metal conductivity is often found in strongly correlated materials such as the high-T superconductors and the Mott insulator–metal transition (IMT) system VO$_2$. The phenomenon of bad-metal conductivity is a central problem in condensed matter physics[1–3].

Here we study bad-metal conductivity and the insulator–metal transition in the nickelates. The nickelate phase diagram features an antiferromagnetic insulator at low T and a paramagnetic metal (PM) at high T. For R = Sm and heavier there is also an intermediate paramagnetic insulator for $T_N < T < T_{IM}$ (T_N = Néel temperature, T_{IM} = IMT temperature)[4]. T_{IM} and the measure of correlation in the metal phase (for example, the suppression of the coherent spectral weight) can be tuned by cation substitution, epitaxial strain, or dimensionality control[4–7]. The nickelates have strong interactions between the charge, spin, orbital and lattice degrees of freedom, and this complexity has obscured the physics of the IMT. Several distinct scenarios have been proposed, including a Mott transition, charge and spin density wave formation, orbital order, and a polaronic insulator[8–14]. Experiments show that the metallic phase is consistent with strong electronic correlations and that the electron–phonon interaction is important, but have not presented a clear explanation of the IMT (refs 5,8,11 and 14). Recently, both total-energy theory and a model Hamiltonian theory have largely reproduced the phase diagram[15,16].

To directly address the apparent breakdown of the lifetime hypothesis in a bad metal we measure a series of samples with controlled levels of disorder. We grow SmNiO$_{3-\delta}$ epitaxial thin films on LaAlO$_3$ by high-pressure sputtering. By varying the sputtering pressure we can control the concentration of oxygen vacancies, producing films with different amounts of disorder[17,18]. Here we report results for five samples, here named SNO1–SNO5, with increasing amounts of disorder. SNO1 is the closest to stoichiometric and displays a sharp IMT. SNO5 is the farthest from stoichiometric and displays a broadened IMT.

In Fig. 1a we present $\sigma_{DC}(T)$ for a conventional metal (Cu), a saturating metal (Ti$_{0.89}$Al$_{0.11}$) and RNiO$_3$. Cu is a good conductor at all T: both σ_{DC} and the fractional slope $-\mathrm{d}\ln(\sigma)/\mathrm{d}T$ (Fig. 1b) are large[19]. Ti$_{0.89}$Al$_{0.11}$ is a saturating metal: σ_{DC} saturates slightly above σ_{MIR} at high T, and the slope $-\mathrm{d}\ln(\sigma)/\mathrm{d}T$ is 30 times smaller than for Cu[1]. We also plot our measurements on SNO3 at high T along with previously published data for RNiO$_3$, all in the PM phase. The published data include R = La, Pr, Nd, Sm and Gd, as well as doped compounds. For all RNiO$_3$, σ_{DC} is below σ_{MIR} at high T. Importantly, the fractional slope $-\mathrm{d}\ln(\sigma)/\mathrm{d}T$ is large for all RNiO$_3$. For SNO3, the fractional slope at 800 K is almost identical to that of Cu, although σ_{DC} is orders of magnitude lower. This means that σ_{DC} does not saturate even as it falls below the MIR limit. Figure 1 establishes RNiO$_3$ as a class of bad metals.

We probe the complex infrared conductivity ($\sigma(E) = \sigma'(E) + \mathrm{i} \times \sigma''(E)$) in the range $E = 25$–$1{,}550$ meV for T between 295

[1]School of Engineering and Applied Sciences, Harvard University, Cambridge, Massachusetts 02138, USA, [2]The James Franck Institute and Department of Physics, The University of Chicago, Chicago, Illinois 60637, USA. [†]Present address: Massachusetts Institute of Technology, Cambridge, Massachusetts 02139, USA. *e-mail: rafael@uchicago.edu
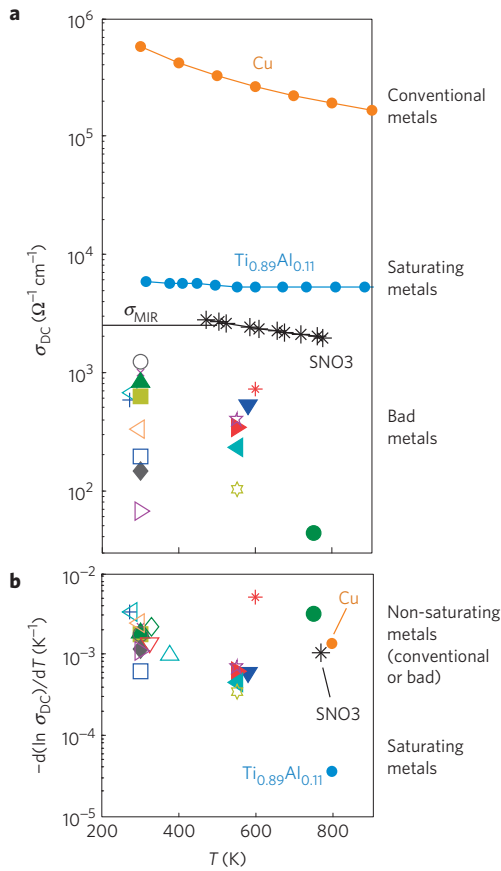
Figure 1 | Bad-metal conductivity in the high-T PM phase of the nickelates.
We show our data for SNO3 along with published data for $RNiO_3$—see Supplementary Information for a key to the symbols. We also show data for a conventional metal (Cu), and a saturating metal ($Ti_{0.89}Al_{0.11}$). **a**, σ_{DC} at high T. There is a clear separation of scales between good metals such as Cu, saturating metals such as $Ti_{0.89}Al_{0.11}$, and bad metals such as $RNiO_3$. For $RNiO_3$ we estimate $\sigma_{MIR} \approx 2,500\ \Omega^{-1}\ cm^{-1}$ (see Supplementary Information). **b**, Fractional derivative $-d\ln(\sigma_{DC})/dT$ corresponding to the data in **a**. Both the bad metals $RNiO_3$ and the conventional metal Cu have a relatively large derivative at high T. In contrast, the saturation of σ_{DC} for $Ti_{0.89}Al_{0.11}$ results in a fractional derivative that is suppressed by a factor of 10–100 compared to Cu and $RNiO_3$. References for published data on $RNiO_3$ are listed in the Supplementary Information, and the points represent the highest reported T.

and 415 K. We measured and analysed 69 complete spectra with varying T and disorder; see Supplementary Information. We show in Fig. 2 the T-dependence of $\sigma'(E)$ for SNO1. The IMT is accompanied by a large increase in spectral weight below 400 meV, only some of which is transferred from the mid-infrared peak near 550 meV. The Ni–O bending and stretching modes (near 35 and 75 meV, respectively) are narrow phonons for $T < T_{IM}$ but merge into the coherent quasiparticle response in the PM phase, becoming strongly damped for $T > T_{IM}$. We identify these phonons by referring to a general analysis of infrared-active phonons in distorted ($Pnma$) perovskites[20]. The Ni–O stretching mode is associated with a breathing distortion of the NiO_6 octahedra, and the bending mode affects the Ni–O–Ni bond angle[12]. The quasiparticles in the PM phase are polarons[11,12]; our data identify the phonon modes that strongly couple with the electronic degrees of freedom. The emergence of a strongly damped phonon response for $T > T_{IM}$ also explains the far-infrared minimum in $\sigma'(\omega)$, which is present in our data and is commonly observed in manganites and bad metals[2].
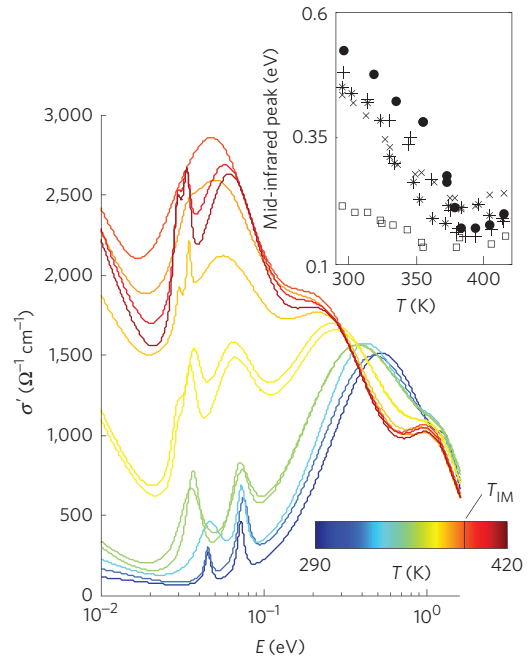

Figure 2 | $\sigma'(E)$ measured across the insulator–metal transition for SNO1.
T_{IM} as measured by the change in slope of $\sigma_{DC}(T)$ is marked on the colour bar. (Inset) T-dependence of the mid-infrared peak position for all five samples SNO1–5 (solid circle, plus, asterisk, cross, open square, respectively).

The mid-infrared peak position (Fig. 2, inset) has the T-dependence expected for an order parameter and has been identified with E_g (ref. 21). However, instead of disappearing in the PM phase it persists as a shoulder on the broad quasiparticle response. We identify this shoulder as a Holstein side band, which is associated with the breakup of a polaron into its constituent phonon and electron degrees of freedom[22]. The connection of the E_g-like feature for $T < T_{IM}$ to the Holstein side band for $T > T_{IM}$ suggests that the IMT is driven by the freezing of the same lattice distortion that is responsible for polaron formation in the PM phase. This is consistent with experiments showing a reduction in symmetry from orthorhombic for $T > T_{IM}$ to monoclinic for $T < T_{IM}$ and with theory showing that the insulating phase is controlled by a period-doubling lattice distortion[15,16,23,24].

The effects of varying T and disorder are captured by the spectral weight:

$$f(E) = \frac{4}{\varepsilon_0 h} \int_0^E dE'\, \sigma'(E') \qquad (1)$$

$f(E)$ counts the quasiparticles that contribute to conductivity at frequencies $\omega < E/\hbar$. $f(E \approx W)$, where W is the conduction band width, measures the effect of strong coupling on the electronic structure. The plasma frequency (Ω_p) is:

$$\Omega_p = \sqrt{\frac{nq^2}{m^*\varepsilon_0}} = \sqrt{f(W)} \qquad (2)$$

where ε_0 is the dielectric permittivity of free space. Strong coupling is taken to be any interaction that significantly alters n or m^* in the PM phase.

We plot in Fig. 3a the T-dependence of $f(E)$ for SNO1. The IMT is accompanied by a steep rise in $f(E)$ in the range $E < 400$ meV, signalling the collapse of E_g and the filling of the conduction band.
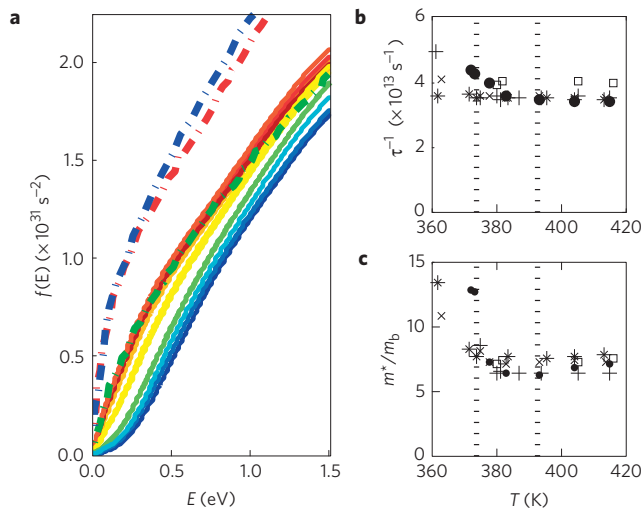
Figure 3 | Spectral weight and extended Drude analysis. a, Solid lines: $f(E)$ for SNO1 across the IMT; the colour scale is the same as in Fig. 2. Broken lines: $f(E)$ for epitaxially strained LaNiO$_3$ (ref. 5; red $=-1.1\%$ strain on LaAlO$_3$, blue $+0.6\%$ strain on (LaAlO$_3$)$_{0.3}$(Sr$_2$AlTaO$_6$)$_{0.7}$; green $=+2.9\%$ strain on DyScO$_3$). **b,c**, Extended Drude analysis for SNO1–SNO5. Symbols are the same as in Fig. 2. Data is significant only in the PM phase ($T > T_{IM}$). $T_{IM} = 394, 386, 380, 387$ and 374 K for SNO1–5, respectively. This range of T_{IM} values is shown by the dashed vertical lines. In **b**, $\tau^{-1}(\omega \to 0)$ is nearly constant for all samples, irrespective of T or disorder. In **c**, $m^*(\omega \to 0)/m_b$ is independent of T for $T > T_{IM}$ for all samples (note the variation in T_{IM}).

Much of the spectral weight transfer comes from high-energy states beyond 1.5 eV, as observed for other RNiO$_3$ (refs 5,8). For $T > T_{IM}$, $f(E)$ is nearly indistinguishable from that measured on 2.9% tensile strained LaNiO$_3$-on-DyScO$_3$ at room temperature

(ref. 5). This suggests a common mechanism for spectral weight suppression for epitaxial strain and rare-earth substitution in RNiO$_3$.

We plot in Fig. 3b–c results from an extended Drude analysis of all samples (Supplementary Information). For an IMT driven by electron–electron correlation m^* diverges as $T \to T_{IM}^+$, as observed in Mott insulators such as VO$_2$ (ref. 3). For SmNiO$_3$ we observe no such mass enhancement approaching T_{IM}. In a conventional metal the effect of adding disorder is to decrease τ, thereby lowering σ_{DC}. For SmNiO$_3$ we see that $\tau(\omega \to 0)$ is nearly constant for all samples, irrespective of the amount of disorder.

According to the standard Drude model if both m^* and τ are constant then a changing σ_{DC} must result from a changing n. In Fig. 4a we overlay $\sigma_{DC}(T)$ for SNO1–5 with Ω_p^2 (Supplementary Information). Ω_p^2 responds to changes in T and disorder in nearly the same way as $\sigma_{DC}(T)$. The correspondence in the PM phase is remarkable: Ω_p^2 decreases in response to increased T or disorder, just as τ does in a conventional metal (Fig. 4b). Figure 4 suggests an explanation for bad-metal conductivity in the nickelates: small changes in T or disorder produce continuous shifts of spectral weight over a large energy scale. This stands in stark contrast to normal metals in which changes in T or disorder affect τ. The defining characteristic of bad metals is the presence of a strong interaction that can continuously shift spectral weight between the conduction band and high-energy states in response to small changes in T and disorder, yielding metallic conductivity below σ_{MIR} while preserving the Drude model and without violating the uncertainty principle[2].

This high-energy scale is provided by the interaction between Ni–O bond covalence and local lattice distortions. The ground state electronic configuration of RNiO$_3$ is nominally $t_{2g}^6 e_g^1$ (Ni^{3+}). However, this ionic representation is inaccurate owing to the strong covalent sigma bonds between Ni e_g and O $2p$ orbitals, and the RNiO$_3$ family are best described as negative charge-transfer valence bond insulators[25,26]. Theory shows that the low-energy density of
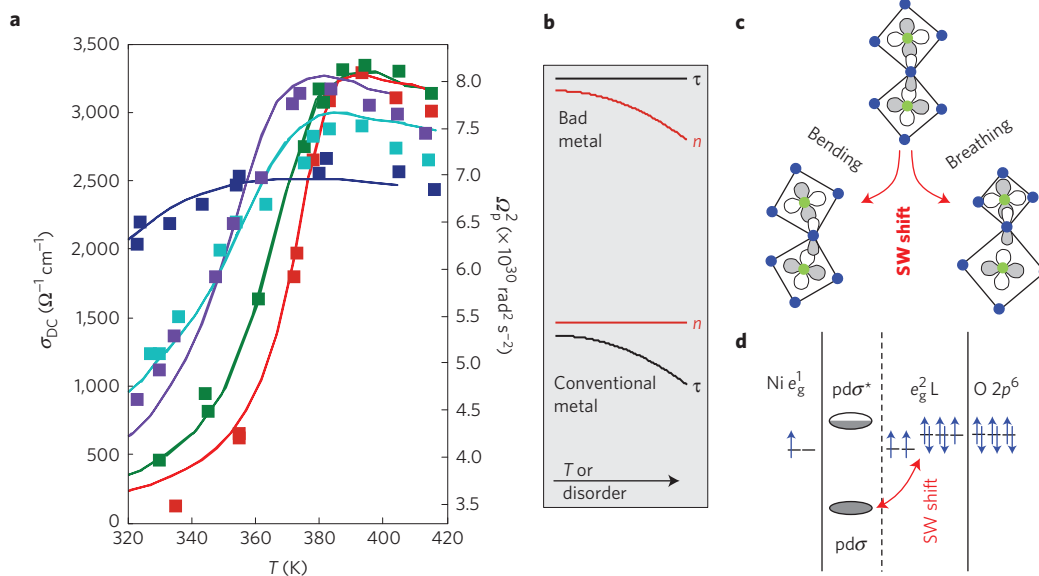

Figure 4 | Spectral weight shifts in response to T, disorder and the insulator–metal transition. a, σ_{DC} (left axis, lines) and Ω_p^2 (right axis, squares) for SNO1–5, (red, green, purple, teal, blue, respectively) as a function of T across T_{IM}. In the PM phase Ω_p^2 decreases in response to increased T or disorder, just as τ does in a conventional metal. **b**, Schematic showing the different responses of a bad metal and a conventional metal to increases in T or disorder. **c**, Schematic of the bending and breathing distortions that shift spectral weight by altering the Ni–O covalence. Blue is O and green is Ni. We draw select Ni e_g and O $2p$ orbitals to illustrate how the distortions affect orbital overlap. **d**, Schematic of the electronic structure; emphasis is on Ni–O bonding and how the Ni e_g and O $2p$ orbitals bond in the covalent and ionic limits. Outer columns correspond to the electronic structure in the nominal $t_{2g}^6 e_g^1$ configuration. The inner-left column shows the limit of covalent Ni–O bonding, with a high energy separating the pdσ and pdσ^* states[15,27]. The inner-right column shows the limits of ionic Ni–O bonding, with the e_g^2 and $\underline{L}$ states separated by the (negative) charge transfer energy.

states (DOS) near the Fermi energy (E_F) is antibonding in character, the bonding DOS is centred at 6–8 eV below E_F, and this separation is the dominant high-energy feature in the electronic structure[15,27]. Importantly, Ni–O covalence is controlled by lattice distortions (Fig. 4c–d)[25]. Overlap between the Ni e_g and O $2p$ orbitals depends on the Ni–O bond lengths and the Ni–O–Ni bond angles. The bond lengths are affected by the breathing mode, and the bond angles are affected by the bending mode. The high-energy electronic structure of RNiO$_3$ is therefore controlled by the local geometry of the NiO$_6$ octahedra.

Both the bending and the breathing modes condense at T_{IM}, resulting in a discrete change in the Ni–O–Ni bond angle and a disproportionation into expanded (Ni1 sites) and contracted (Ni2 sites) octahedra[14–16,23,24]. This affects the Ni–O covalence and transfers spectral weight over large energies, as observed experimentally[8]. In the insulating phases the Ni1 sites are closer to the ionic limit $t_{2g}^6 e_g^2 \underline{L}$ ($\underline{L}$ denotes a 'ligand hole' on an oxygen orbital), with spin quantum number $S = 1$. The Ni2 sites are closer to the covalent limit, with electrons in bonding orbitals forming $S = 0$ singlets[13–15]. E_g is approximately ten times smaller than the large-energy scales in the system, and results from period doubling that splits the low-energy DOS (refs 9,13,15). The low-energy DOS is predominantly $\underline{L}$-like; transport through the e_g^2 manifold is suppressed by the Hubbard intra-orbital electron–electron Coulomb interaction.

In the PM phase, spectral weight is continuously redistributed in response to changes in T or disorder by dynamic electron–phonon interactions, as suggested by the strongly damped bending and breathing modes and by the observation of dynamic Ni1–Ni2 fluctuations above T_{IM} (ref. 24). It is a challenge to theory to fully describe the electron–phonon interaction in the PM phase. A full description will probably include a pseudogap in the metallic DOS. It would be interesting to study the effects of controllably introducing different types of disorder on the spectral weight and the lattice distortion in the PM phase of the nickelates.

The shifting of spectral weight in the PM phase is also seen in Mott–Hubbard materials[2]. We conclude that a strong interaction that can shift spectral weight over a large energy scale is necessary for bad-metal conductivity, but that the identity of this interaction may vary. Notably, our work describes bad-metal conductivity in a material system in which the Hubbard interaction is of secondary importance. Both total energy and model Hamiltonian theory agree that the Hubbard interaction does not control the phase diagram, it does not significantly affect the electronic structure, and is not the driving force for the IMT in the nickelates[15,16,27]. Our results confirm the primary importance of the electron–phonon interaction and rule out a conventional Mott–Hubbard IMT. This is consistent with the Zaanen–Sawatzky–Allen classification of transition metal oxides, wherein for late transition metals (including Ni) the Hubbard energy is so large that it only indirectly controls the phase diagram[28].

References

1. Gunnarsson, O., Calandra, M. & Han, J. E. Colloquium: Saturation of electrical resistivity. *Rev. Mod. Phys.* **75,** 1085–1099 (2003).
2. Hussey, N. E., Takenaka, K. & Takagi, H. Universality of the Mott–Ioffe–Regel limit in metals. *Phil. Mag.* **84,** 2847–2864 (2004).
3. Qazilbash, M. M. *et al.* Correlated metallic state of vanadium dioxide. *Phys. Rev. B* **74,** 205118 (2006).
4. Zhou, J-S., Goodenough, J. B. & Dabrowski, B. Transition from Curie–Weiss to enhanced Pauli paramagnetism in RNiO$_3$ (R = La,Pr,... Gd). *Phys. Rev. B* **67,** 020404 (2003).
5. Ouellette, D. G. *et al.* Optical conductivity of LaNiO$_3$: Coherent transport and correlation driven mass enhancement. *Phys. Rev. B* **82,** 165112 (2010).
6. Boris, A. V. *et al.* Dimensionality control of electronic phase transitions in nickel–oxide superlattices. *Science* **332,** 937–940 (2011).
7. Liu, J. *et al.* Heterointerface engineered electronic and magnetic phases of NdNiO$_3$ thin films. *Nature Commun.* **4,** 2714 (2013).
8. Stewart, M. K., Liu, J., Kareev, M., Chakhalian, J. & Basov, D. N. Mott physics near the insulator-to-metal transition in NdNiO$_3$. *Phys. Rev. Lett.* **107,** 176401 (2011).
9. Mazin, I. I. *et al.* Charge ordering as alternative to Jahn-Teller distortion. *Phys. Rev. Lett.* **98,** 176406 (2007).
10. Lee, S., Chen, R. & Balents, L. Landau theory of charge and spin ordering in the nickelates. *Phys. Rev. Lett.* **106,** 016405 (2011).
11. Medarde, M., Lacorre, P., Conder, K., Fauth, F. & Furrer, A. Giant ^{16}O-^{18}O isotope effect on the metal-insulator transition of RNiO$_3$ perovskites (R = Rare Earth). *Phys. Rev. Lett.* **80,** 2397–2400 (1998).
12. Mroginski, M. A., Massa, N. E., Salva, H., Alonso, J. A. & Martínez-Lope, M. J. Metal–insulator phase transitions of SmNiO$_3$ and PrNiO$_3$: Electrons in a polaronic medium. *Phys. Rev. B* **60,** 5304–5311 (1999).
13. Chakhalian, J. *et al.* Asymmetric orbital-lattice interactions in ultrathin correlated oxide films. *Phys. Rev. Lett.* **107,** 116805 (2011).
14. Goodenough, J., Zhou, J-S., Rivadulla, F. & Winkler, E. Bond-length fluctuations in transition-metal oxoperovskites. *J. Solid State Chem.* **175,** 116–123 (2003).
15. Park, H., Millis, A. J. & Marianetti, C. A. Site-selective Mott transition in rare-earth-element nickelates. *Phys. Rev. Lett.* **109,** 156402 (2012).
16. Lau, B. & Millis, A. J. Theory of the magnetic and metal-insulator transitions in RNiO$_3$ bulk and layered structures. *Phys. Rev. Lett.* **110,** 126404 (2013).
17. Ha, S. D., Otaki, M., Jaramillo, R., Podpirka, A. & Ramanathan, S. Stable metal–insulator transition in epitaxial SmNiO$_3$ thin films. *J. Solid State Chem.* **190,** 233–237 (2012).
18. Ha, S. D. *et al.* Hall effect measurements on epitaxial SmNiO$_3$ thin films and implications for antiferromagnetism. *Phys. Rev. B* **87,** 125150 (2013).
19. *Electrical Resistivity, Kondo and Spin Fluctuation Systems, Spin Glasses and Thermopower. Vol. 15* (Springer, 1982).
20. Nakagawa, I., Tsuchida, A. & Shimanouchi, T. Infrared transmission spectrum and lattice vibration analysis of some perovskite fluorides. *J. Chem. Phys.* **47,** 982–989 (1967).
21. Katsufuji, T., Okimoto, Y., Arima, T., Tokura, Y. & Torrance, J. B. Optical spectroscopy of the metal–insulator transition in NdNiO$_3$. *Phys. Rev. B* **51,** 4830–4835 (1995).
22. Emin, D. Optical properties of large and small polarons and bipolarons. *Phys. Rev. B* **48,** 13691–13702 (1993).
23. Alonso, J. A. *et al.* Charge disproportionation in RNiO$_3$ (R = Tm, Yb) perovskites observed in situ by neutron diffraction and ^{57}Fe probe Mössbauer spectroscopy. *Phys. Rev. B* **87,** 184111 (2013).
24. Medarde, M. *et al.* Charge disproportionation in RNiO$_3$ perovskites (R = rare earth) from high-resolution x-ray absorption spectroscopy. *Phys. Rev. B* **80,** 245105 (2009).
25. Mizokawa, T. *et al.* Origin of the band gap in the negative charge-transfer-energy compound NaCuO$_3$. *Phys. Rev. Lett.* **67,** 1638–1641 (1991).
26. Mizokawa, T. *et al.* Electronic structure of PrNiO$_3$ studied by photoemission and x-ray-absorption spectroscopy: Band gap and orbital ordering. *Phys. Rev. B* **52,** 13865–13873 (1995).
27. Wang, X. *et al.* Covalency, double-counting, and the metal-insulator phase diagram in transition metal oxides. *Phys. Rev. B* **86,** 195136 (2012).
28. Zaanen, J., Sawatzky, G. A. & Allen, J. W. Band gaps and electronic structure of transition-metal compounds. *Phys. Rev. Lett.* **55,** 418–421 (1985).

Acknowledgements

Author contributions

R.J. conceived of, planned and executed the experiments, analysed and interpreted the results, and wrote the manuscript. S.D.H. grew the samples and edited the manuscript. D.M.S. performed the low-temperature electronic transport measurements. S.R. provided support and technical discussions.

Additional information

Supplementary information is available in the online version of the paper. Reprints and permissions information is available online at www.nature.com/reprints. Correspondence and requests for materials should be addressed to R.J.

Competing financial interests

The authors declare no competing financial interests.